JACS
JOURNAL OF THE AMERICAN CHEMICAL SOCIETY

Communication

pubs.acs.org/JACS

Nanostructured Tin Catalysts for Selective Electrochemical Reduction of Carbon Dioxide to Formate

Sheng Zhang, Peng Kang, and Thomas J. Meyer*

Department of Chemistry, University of North Carolina at Chapel Hill, Chapel Hill, North Carolina 27599, United States

Supporting Information

ABSTRACT: High surface area tin oxide nanocrystals prepared by a facile hydrothermal method are evaluated as electrocatalysts toward CO_2 reduction to formate. At these novel nanostructured tin catalysts, CO_2 reduction occurs selectively to formate at overpotentials as low as ~340 mV. In aqueous $NaHCO_3$ solutions, maximum Faradaic efficiencies for formate production of >93% have been reached with high stability and current densities of >10 mA/cm^2 on graphene supports. The notable reactivity toward CO_2 reduction achieved here may arise from a compromise between the strength of the interaction between $CO_2^{\bullet-}$ and the nanoscale tin surface and subsequent kinetic activation toward protonation and further reduction.

The increasing carbon dioxide content in the atmosphere has been cited as a major contributor to the greenhouse effect and global warming.[1] Electrochemical or photoelectrochemical reduction of CO_2 could provide an attractive solution to this climate issue, with CO_2 converted into useful fuels and utilized as a chemical feedstock. It is also an energy storage strategy, with solar or electrical energy stored as chemical energy in a reduced carbon product.[2] A number of homogeneous and heterogeneous catalysts have been evaluated for electrochemical CO_2 reduction, including metal electrodes.[3] Tin electrodes have been found to selectively convert CO_2 to formate and formic acid,[4] with the acid a good candidate as an anode fuel for fuel cells[5] and a promising material as a hydrogen carrier. Electrodes of Pb, Hg, In, Cd, and Tl are also able to promote reduction of CO_2 to formate but are highly toxic, expensive, or both.

Formate production by electrochemical reduction of CO_2 at tin electrodes has been reported with a wide range of Faradaic efficiencies. Lee et al. loaded tin particles on carbon paper by electrochemical reduction and found a Faradaic efficiency of only 18% for formate,[6] while a value of 80% was reported by Sridhar et al. at a similarly electrochemically reduced tin electrode.[7] Kanan et al. reported a significantly increased Faradaic efficiency for formate on tin/tin oxide electrodes (~58%) for CO_2 reduction compared to tin foil (~19%),[3d] while Hori et al. found a Faradaic efficiency for formate on tin foil of ~88%.[3g] These results point to an electrocatalytic activity that is highly dependent on structure, morphology, and electrolysis conditions.[3d,8]

We report here the results of an electrochemical study on the reduction of CO_2 at ultrafine nanoscale tin oxide with controlled particle sizes. These tin oxide nanoparticles (NPs) were synthesized by the hydrothermal method. To maximize surface area, they were loaded onto high surface area carbon supports (carbon black and graphene), with the added advantage of utilizing their 3D porous structures to facilitate CO_2 transport and reduction. The as-prepared tin oxide NP surfaces were characterized as tin(IV) oxide (SnO_2) and shown to be quickly and efficiently reduced to the metal at an onset potential of ~1 V vs SCE. We find a notable size dependence on the efficiency of CO_2 reduction to formate at the reduced nanoscale tin oxide catalyst surfaces. Efficiencies are maximized on 5 nm particles, reaching a maximum Faradaic efficiency for formate production of >93%. These catalysts are very stable during electrolysis and can continue producing formate for at least 18 h. Electrocatalytic activity toward CO_2 reduction can be tuned by morphology and tuning the electronic structure of the Sn catalyst.

Synthesis and Characterization of Nanoscale Tin Oxide. Tin oxide NPs were synthesized by a modification of a facile hydrothermal method (see Supporting Information for details).[9] Figure 1a,b shows TEM images of synthesized tin oxide NPs loaded onto carbon black (~30 nm in diameter), at different resolutions, illustrating tin oxide NPs (small black dots) of ~5 nm average diameter, uniformly deposited on the surface of the carbon black. In the high-resolution TEM images in Figure S1,

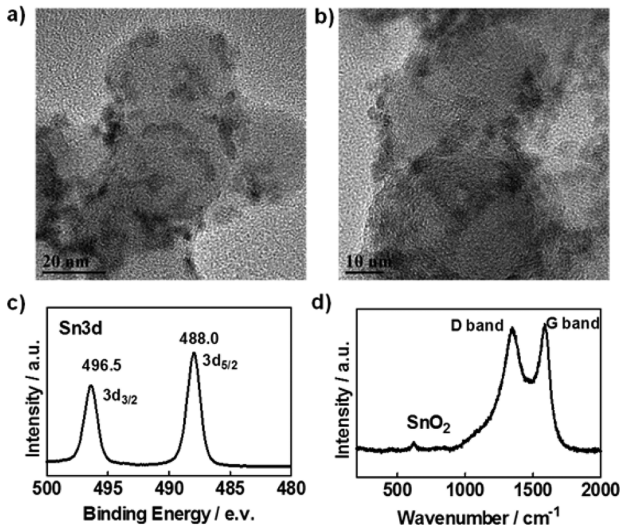

Figure 1. Transmission electron microscopy images (a,b), high-resolution Sn3d XPS spectrum (c), and Raman spectrum (d) of nanoscale tin oxide on carbon black.

Received: November 7, 2013
Published: January 13, 2014

ACS Publications © 2014 American Chemical Society

dx.doi.org/10.1021/ja4113885 | J. Am. Chem. Soc. 2014, 136, 1734−1737

obvious lattice fringes of tin oxide are observed and average lattice spacing of ~0.335 nm is measured, consistent with the (110) plane of rutile Sn(IV) oxide NPs.[10] The available evidence is all consistent with formation of Sn(IV) oxide (SnO_2) NPs. A formation mechanism is proposed in Figure S2. It features prior coordination to the $SnCl_2$ precursor by ethylene glycol and water with displacement of Cl^-. At high temperatures aquated Sn(II) forms $Sn(OH)_2$, which is converted into SnO and further oxidized by oxygen in the air to give nano-SnO_2.

The high-resolution Sn3d XPS spectrum in Figure 1c exhibits binding energies at 496.5 and 488.0 eV that can be assigned to $Sn3d_{3/2}$ and $Sn3d_{5/2}$ ionizations, respectively. These energies are consistent with Sn(IV) bound to oxygen in SnO_2.[11] In the high-resolution XPS valence band spectrum in Figure S3b, three binding energies appear above 5 eV, consistent with SnO_2.[12] In the Raman spectrum in Figure 1d, characteristic bands appear at 1350 and 1580 cm^{-1}, which arise from the D and G bands of carbon black, respectively. The scattering feature at ~630 cm^{-1} is a characteristic of rutile SnO_2 nanocrystals.[13] The three intense diffraction peaks in the XRD pattern shown in Figure S3a at 2θ = 26.2°, 33.7°, and 51.2° can be indexed as the (110), (101), and (211) planes of the polycrystalline rutile SnO_2 structure, respectively.[14] The average particle size of the SnO_2 nanocrystals can be calculated by using the Scherrer equation[15] to be ~4.8 nm, which is slightly less than that from the TEM data.

Electrocatalytic Reduction of CO_2. Electrocatalytic CO_2 reduction by nano-SnO_2 was evaluated in 0.1 M $NaHCO_3$ aqueous solutions. In the linear sweep voltammetric (LSV) scans in Figure S5, a reduction peak appears at −1.0 V in initial scans. It arises from reduction of SnO_2 NPs[16] and disappears after 50 cycles from −1 to −1.8 V, indicative of reduction on carbon black. It should be noted that all LSV scans and controlled potential electrolysis experiments reported here were conducted on reduced nano-SnO_2 catalysts. A small amount of tin oxide might still persist within the core of the reduced Sn catalyst. However, due to lack of access to electrolyte, the residual tin oxide presumably does not contribute to CO_2 reduction.

Figure 2 illustrates single reductive LSV scans at a reduced nano-SnO_2/carbon black coated glassy carbon electrode (0.07 cm^2) in 0.1 M $NaHCO_3$. They are compared to a bare glassy carbon electrode, carbon black, and electrodeposited ~200 nm

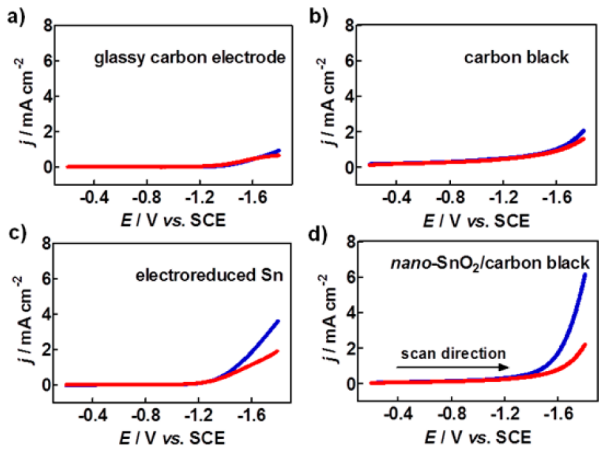

Figure 2. Single reductive linear sweep voltammetric scans at 50 mV/s under N_2 (red line) and in a CO_2 (1 atm, blue line)-saturated solution in aqueous 0.1 M $NaHCO_3$ at bare glassy carbon electrode (a), glassy carbon electrode with carbon black (b), electrodeposited tin particles (c), and reduced nano-SnO_2/carbon black (d).

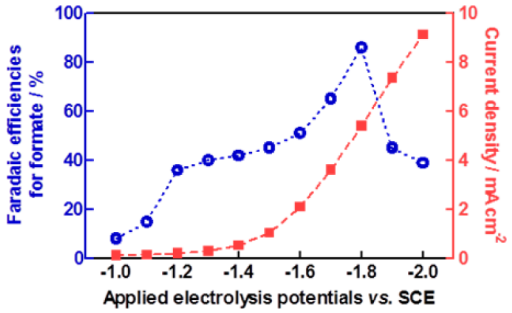

Figure 3. Applied electrolysis potential dependence of total current densities (red squares) and Faradaic efficiencies (blue circles) for formate production on reduced nano-SnO_2 loaded on carbon black.

tin NPs on glassy carbon. The LSV scans in Figure 2a,b show that the glassy carbon electrode and carbon black have negligible catalytic currents for CO_2 reduction. The scans in Figure 2c provide obvious evidence for catalytic reduction of CO_2 at electrodeposited tin NPs with a current density of 3.6 mA/cm^2 at −1.8 V in solutions saturated in CO_2. The current level is nearly twice that of the background but still comparable to that of commercial tin foil under CO_2 (Figure S6). By comparison, the current density in Figure 2d for the reduced nano-SnO_2/carbon black electrode reached 6.2 mA/cm^2 at −1.8 V. When these SnO_2 NPs were loaded onto graphene, their performance for CO_2 reduction was further enhanced, with current densities of 13.1 mA/cm^2 reached under the same conditions (see Figure 5d). The specific current densities (with catalytic currents normalized to the mass of Sn catalysts) were calculated to be 266, 126, and 2 A/g for nano-SnO_2/graphene, nano-SnO_2/carbon black, and electrodeposited tin NPs, respectively.

Controlled potential electrolyses were performed to investigate the effect of applied potentials on Faradaic efficiencies for formate production at reduced nano-SnO_2/carbon black electrodes. Figure 3 illustrates the applied electrolysis potential dependence of current densities and Faradaic efficiencies for formate production. As expected, current densities increase with applied overpotentials. Formate anion as an electrolysis product was detected by ^1H NMR.

The results in Figure 3 show that current efficiencies for formate reach a maximum (86.2%) at moderately negative potentials (−1.8 V) but decrease at more negative potentials. Given $E^{\circ\prime}$ = −0.67 V vs SCE for the $CO_2/HCOO^-$ couple, the overpotential for CO_2 reduction under these conditions is 1.13 V. Analysis of gaseous products (Varian 450-GC) after electrolysis revealed that hydrogen was produced at all applied potentials, along with small amounts of carbon monoxide (2−6%). At applied potentials more positive than −1.8 V, slow reduction to formate occurs. At very negative potentials, currents increase and the Faradaic efficiency for formate production decreases due to an increase in hydrogen evolution, which competes with CO_2 reduction to formate under these conditions.

As shown in Figure S7, controlled potential electrolysis of nano-SnO_2/carbon black at −1.8 V for 18 h resulted in a steady-state catalytic current density of ~5.4 mA/cm^2. TEM images in Figure S8 and LSV curves in Figure S9 at the reduced nano-SnO_2/carbon black electrode after electrolysis suggest that the morphology and catalytic properties of the SnO_2 NPs are essentially unchanged. It is worth noting that even at the very low overpotential of ~0.34 V (E_{app} = −1 V vs SCE, −0.76 V vs SHE, or −0.36 V vs RHE), formate was still produced, although with a relatively low current efficiency of ~8%.

dx.doi.org/10.1021/ja4113885 | J. Am. Chem. Soc. 2014, 136, 1734−1737

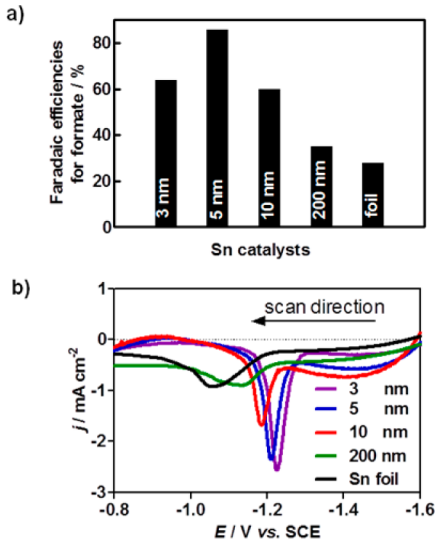

Figure 4. (a) Particle size dependence of Faradaic efficiencies for CO_2 reduction to formate on Sn catalysts. (b) Single oxidative LSV scans at 50 mV/s in N_2-saturated 0.1 M NaOH at Sn catalysts of varying morphologies, illustrating surface adsorption of OH^- accompanying oxidation to surface tin oxide.

Electrolysis at SnO_2/graphene was also conducted at −1.8 V for 18 h in CO_2 saturated 0.1 M $NaHCO_3$ (Figure S13). Current densities increased to ∼10.2 mA/cm^2 compared to carbon black as the substrate. More notably, the Faradaic efficiency for formate production at the reduced nano-SnO_2/graphene increased to 93.6%.

CO_2 reduction efficiencies on Sn catalysts depend on particle size. As shown in Figure 4a, Faradaic efficiencies for formate production at −1.8 V at Sn electrodes with varying morphologies show that the maximum current efficiency occurs at 5 nm tin oxide NPs. The same trend was observed at −1.6 and −2 V (see Table S1 for details). Morphologies for these samples are shown in Figure S10. To explore a possible role for adsorption of the reduced intermediate $CO_2^{\bullet-}$ during CO_2 catalytic reduction cycles, and how it varies with particle size, we examined adsorption of OH^- as a surrogate for $CO_2^{\bullet-}$ as a function of particle size.[17] In these experiments, the current response was monitored following single oxidative LSV scans beginning at −1.6 V vs SCE through the surface wave for Sn(0) oxidation to Sn(II). Based on the data in Figure 4b, the potential for surface adsorption of OH^- is lowest for the 3 nm tin oxide NPs and increases with increasing particle size. The size dependence suggests an enhanced binding energy for OH^- on Sn(II)-doped surfaces which is maximized for the 3 nm tin oxide particles.

In comparing the data in Figure 4, enhanced surface binding does not correlate with enhanced electrocatalytic activity toward CO_2 reduction, with the maximum efficiency reached for 5 nm particles. A related phenomenon has been observed for oxygen reduction catalysis at metal electrodes by Adzic et al. Their results show that in oxygen reduction, fissioning of the O−O bond is inhibited for catalytic surfaces with weak affinities and binding energies for atomic oxygen and that O−H bond formation is difficult on catalytic surfaces with high binding energies.[18] They concluded that an optimal oxygen reduction catalyst should achieve a balance between O−O bond breaking and O−H bond formation. Experimentally, oxygen reduction activity is maximized for catalytic surfaces with moderate atomic oxygen atom binding energies. For CO_2 reduction, maximized efficiencies for 5 nm tin oxide nanocrystals may arise from an optimized affinity toward surface binding of a key intermediate or intermediates during CO_2 reduction. In particular, adsorption of electrogenerated $CO_2^{\bullet-}$ may play a key role in the initial step with E° = −2.21 V vs SCE in dry dimethylformamide for the $CO_2/CO_2^{\bullet-}$ couple.[19] An additional factor may be that competitive hydrogen evolution is suppressed at 5 nm tin oxide nanocrystals.

A possible CO_2 reduction mechanism on Sn is illustrated in eqs 1−5. In the reaction sequence, eq 3 is presumably the rate-determining step (RDS). This assignment is supported by the results in Figure S11 showing that catalytic current densities for CO_2 reduction increase essentially linearly with the concentrations of HCO_3^-. Additional evidence is provided by the Tafel slope (Figure S12) of ∼70 mV dec^{-1}, which is close to 59 mV dec^{-1}. This suggests a mechanism involving a chemical RDS.[3d] These kinetics are consistent with electron transfer and adsorption of $CO_2^{\bullet-}$ followed by rate-limiting proton transfer from HCO_3^-. Proton transfer may trigger a second electron transfer from the electrode to give the adsorbed formate product. Alternately, concerted electron−proton reduction of adsorbed $CO_2^{\bullet-}$ with electron transfer from the electrode occurring in concert with proton transfer from HCO_3^-, eq 3, may occur, with the advantage of giving adsorbed formate directly.

$$CO_2(\text{solution}) \rightarrow CO_2(\text{ads}) \quad (1)$$

$$CO_2(\text{ads}) + e^- \rightarrow CO_2^{\bullet-}(\text{ads}) \quad (2)$$

$$CO_2^{\bullet-}(\text{ads}) + HCO_3^- + e^- \rightarrow HCO_2^-(\text{ads}) + CO_3^{2-} \quad (3)$$

$$HCO_2^-(\text{ads}) \rightarrow HCO_2^-(\text{solution}) \quad (4)$$

$$CO_3^{2-} + CO_2 + H_2O \rightarrow 2HCO_3^- \quad (5)$$

In these mechanisms surface adsorption plays a role in CO_2 reduction. Surface stabilization by adsorption would increase the barrier to further reduction and protonation of $CO_2^{\bullet-}$, with weak adsorption decreasing the activating effect of surface binding. Experimentally, the interplay between the two leads to maximized efficiencies for 5 nm particles.

The electronic structure of the nanoscale tin catalyst may also play an important role with catalysis maximized on graphene as the support. Graphene is a two-dimensional, one-atom-thick sp^2-bonded delocalized carbon substrate. Strong electronic interactions between graphene and added metal NPs can modify the electronic structure of the latter and influence surface molecular adsorption and reactivity.[15]

The TEM images in Figures 5a and S13 show ∼5 nm nano-SnO_2 particles that are loaded on the surface of graphene. In the high-resolution TEM image in Figure 5b, clear lattice fringes are observed with average lattice spacing of ∼0.335 nm for the (110) plane of rutile nano-SnO_2 materials. SnO_2 NPs in SnO_2/carbon black and SnO_2/graphene were prepared by the same method with the same particle size, crystallinity (Figure S14), and catalyst loading (∼30 wt% as determined by energy-dispersive spectroscopy). However, as shown in Figure S15, at −1.8 V, higher Faradaic efficiencies for formate production (93.6%) were obtained at reduced nano-SnO_2/graphene, nearly twice the current density (10.2 mA/cm^2) as for SnO_2/carbon black.

The difference in catalytic activity may be a consequence of differences in the influence of electronic perturbations on Sn particle electronic structure on the two supports. From the high resolution Sn3d XPS spectrum in Figure 5c, Sn 3d XPS binding energies appear at 496.2 and 487.7 eV, respectively, shifted 0.3 eV to lower energy compared to SnO_2/carbon black. The negative

dx.doi.org/10.1021/ja4113885 | J. Am. Chem. Soc. 2014, 136, 1734−1737

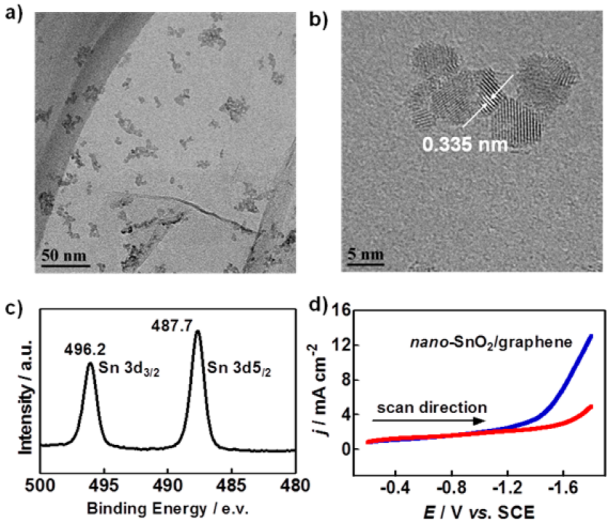

Figure 5. TEM image (a), high-resolution TEM image (b) showing obvious lattice fringe, Sn3d XPS spectrum (c) of SnO_2 nanoparticles on graphene, and single reductive LSV scans (d) at 50 mV/s under N_2 (red line) and in a CO_2 (blue line)-saturated solution at the reduced nano-SnO_2/graphene in aqueous 0.1 M $NaHCO_3$.

shift in binding energies may arise from the stronger electron donating ability of graphene compared to carbon black.[20] In a recent study it was shown that adsorption of CO_2 and $CO_2^{\bullet-}$ is promoted and CO_2 reduction facilitated at negatively charged metal NPs.[21] Based on this observation, it is reasonable to propose that extensive electron donation from graphene to tin oxide is the source of the negative shift in Sn3d XPS binding energies. This electronic interaction leads to enhanced electronic donation, promoting adsorption of CO_2 and $CO_2^{\bullet-}$ and facilitating CO_2 reduction at the Sn surface.

An important result of this study is the observation that, by controlling the size of tin oxide NPs on carbon supports, overpotentials as low as ~340 mV can be achieved for CO_2 reduction to $HCOO^-$, with significant enhancements in both current density and efficiency. In CO_2-saturated aqueous $NaHCO_3$ solutions, maximum Faradaic efficiencies for formate production of >93% have been reached with current densities of over 10 mA/cm^2 on high surface area graphene supports. The reduced nanoscale tin oxide catalysts are highly stable during controlled potential electrolysis, and it should be possible to achieve current density enhancements of 1−2 orders of magnitude by using flow cell or gas diffusion electrodes.

The reactivity toward CO_2 reduction achieved here is notable. It may arise from a compromise between the strength of the interaction between $CO_2^{\bullet-}$ with the nanoscale tin surface and its subsequent kinetic activation toward protonation and further reduction. With the graphene support there may also be a role for electronic interactions with the underlying graphene substrate. In any case, our results demonstrate important roles for catalyst morphology and electronic structure in the electrocatalytic reduction of CO_2.

■ ASSOCIATED CONTENT

Ⓢ Supporting Information

Materials preparation, electrochemical measurements, and physical characterizations. This material is available free of charge via the Internet at http://pubs.acs.org.

■ AUTHOR INFORMATION

Corresponding Author

tjmeyer@unc.edu

Notes

The authors declare no competing financial interest.

■ ACKNOWLEDGMENTS

This research was wholly supported by the UNC EFRC: Center for Solar Fuels, an Energy Frontier Research Center funded by the U.S. Department of Energy Office of Science, Office of Basic Energy Sciences, under Award Number DE-SC0001011.

■ REFERENCES

(1) Karl, T. R.; Trenberth, K. E. *Science* **2003**, *302*, 1719.

(2) (a) Kang, P.; Cheng, C.; Chen, Z.; Schauer, C. K.; Meyer, T. J.; Brookhart, M. *J. Am. Chem. Soc.* **2012**, *134*, 5500. (b) Benson, E. E.; Kubiak, C. P.; Sathrum, A. J.; Smieja, J. M. *Chem. Soc. Rev.* **2009**, *38*, 89.

(3) (a) Kang, P.; Meyer, T. J.; Brookhart, M. *Chem. Sci.* **2013**, *4*, 3497. (b) Chen, Z.; Kang, P.; Zhang, M.-T.; Stoner, B. R.; Meyer, T. J. *Energy Environ. Sci.* **2013**, *6*, 813. (c) Rosen, B. A.; Salehi-Khojin, A.; Thorson, M. R.; Zhu, W.; Whipple, D. T.; Kenis, P. J. A.; Masel, R. I. *Science* **2011**, *334*, 643. (d) Chen, Y.; Kanan, M. W. *J. Am. Chem. Soc.* **2012**, *134*, 1986. (e) Chen, Y.; Li, C. W.; Kanan, M. W. *J. Am. Chem. Soc.* **2012**, *134*, 19969. (f) DiMeglio, J. L.; Rosenthal, J. *J. Am. Chem. Soc.* **2013**, *135*, 8798. (g) Hori, Y.; Wakebe, H.; Tsukamoto, T.; Koga, O. *Electrochim. Acta* **1994**, *39*, 1833. (h) Kuhl, K. P.; Cave, E. R.; Abram, D. N.; Jaramillo, T. F. *Energy Environ. Sci.* **2012**, *5*, 7050.

(4) (a) Li, H.; Oloman, C. *J. Appl. Electrochem.* **2006**, *36*, 1105. (b) Köleli, F.; Atilan, T.; Palamut, N.; Gizir, A. M.; Aydin, R.; Hamann, C. H. *J. Appl. Electrochem.* **2003**, *33*, 447.

(5) Zhang, S.; Shao, Y.; Yin, G.; Lin, Y. *Angew. Chem., Int. Ed.* **2010**, *49*, 2211.

(6) Machunda, R. L.; Ju, H.; Lee, J. *Curr. Appl. Phys.* **2011**, *11*, 986.

(7) Agarwal, A. S.; Zhai, Y.; Hill, D.; Sridhar, N. *ChemSusChem* **2011**, *4*, 1301.

(8) Wu, J. J.; Risalvato, F. G.; Ke, F. S.; Pellechia, P. J.; Zhou, X. D. *J. Electrochem. Soc.* **2012**, *159*, F353.

(9) Jiang, L.; Sun, G.; Zhou, Z.; Sun, S.; Wang, Q.; Yan, S.; Li, H.; Tian, J.; Guo, J.; Zhou, B.; Xin, Q. *J. Phys. Chem. B* **2005**, *109*, 8774.

(10) Wang, D.; Kou, R.; Choi, D.; Yang, Z.; Nie, Z.; Li, J.; Saraf, L. V.; Hu, D.; Zhang, J.; Graff, G. L.; Liu, J.; Pope, M. A.; Aksay, I. A. *ACS Nano* **2010**, *4*, 1587.

(11) Wang, C.; Wu, Q.; Ge, H. L.; Shang, T.; Jiang, J. Z. *Nanotechnology* **2012**, *23*, 075704.

(12) Kover, L.; Moretti, G.; Kovacs, Z.; Sanjines, R.; Csemy, I.; Margaritondo, G.; Palinkas, J.; Adachi, H. *J. Vac. Sci. Technol. A* **1995**, *13*, 1382.

(13) Wang, Y.; Aponte, M.; Leon, N.; Ramos, I.; Furlan, R.; Evoy, S.; Santiago-Aviles, J. J. *Semicond. Sci. Technol.* **2004**, *19*, 1057.

(14) Guo, Q.; Zheng, Z.; Gao, H.; Ma, J.; Qin, X. *J. Power Sources* **2013**, *240*, 149.

(15) Zhang, S.; Shao, Y.; Liao, H.-G.; Liu, J.; Aksay, I. A.; Yin, G.; Lin, Y. *Chem. Mater.* **2011**, *23*, 1079.

(16) Nakayama, S.; Sugihara, T.; Matsumoto, J.; Notoya, T.; Osakai, T. *J. Electrochem. Soc.* **2011**, *158*, C341.

(17) Salehi-Khojin, A.; Jhong, H.-R. M.; Rosen, B. A.; Zhu, W.; Ma, S.; Kenis, P. J. A.; Masel, R. I. *J. Phys. Chem. C* **2012**, *117*, 1627.

(18) Zhang, J.; Vukmirovic, M. B.; Xu, Y.; Mavrikakis, M.; Adzic, R. R. *Angew. Chem., Int. Ed.* **2005**, *44*, 2132.

(19) Lamy, E.; Nadjo, L.; Savéant, J. M. *J. Electroanal. Chem. Interfacial Electrochem.* **1977**, *78*, 403.

(20) (a) Yoo, E.; Okata, T.; Akita, T.; Kohyama, M.; Nakamura, J.; Honma, I. *Nano Lett.* **2009**, *9*, 2255. (b) Zhang, S.; Shao, Y.; Liao, H.; Engelhard, M. H.; Yin, G.; Lin, Y. *ACS Nano* **2011**, *5*, 1785.

(21) Kauffman, D. R.; Alfonso, D.; Matranga, C.; Qian, H.; Jin, R. *J. Am. Chem. Soc.* **2012**, *134*, 10237.